

Tension-driven three-dimensional printing of free-standing Field's metal structures

Received: 2 June 2023

Accepted: 17 June 2024

Published online: 25 July 2024



Shaohua Ling^{1,2,9}, Xi Tian^{3,9}, Qihang Zeng^{4,5}, Zhihang Qin^{1,2},
Selman A. Kurt⁵, Yu Jun Tan², Jerry Y. H. Fuh², Zhuangjian Liu⁶,
Michael D. Dickey⁷, John S. Ho^{4,5,8}✉ & Benjamin C. K. Tee^{1,4,8}✉

The direct writing of complex three-dimensional (3D) metallic structures is of use in the development of advanced electronics. However, conventional direct ink writing primarily uses composite inks that have low electrical conductivity and require support materials to create 3D architectures. Here we show that Field's metal—a eutectic alloy with a relatively low melting point—can be 3D printed using a process in which tension between the molten metal in a nozzle and the leading edge of the printed part allows 3D structures to be directly written. The use of tension avoids using external pressure for extrusion (which can cause beading of the printed structure), allowing uniform and smooth microwire structures to be printed on various substrates with speeds of up to 100 mm s⁻¹. We use the approach to print various free-standing 3D structures—including vertical letters, a cubic framework and scalable helixes—without post-treatment, and the resulting Field's metal structures can offer electrical conductivity of 2×10^4 S cm⁻¹, self-healing capability and recyclability. We also use the technique to print a 3D circuit for wearable battery-free temperature sensing, hemispherical helical antennas for wireless vital sign monitoring and 3D metamaterials for electromagnetic-wave manipulation.

Compared with conventional two-dimensional (2D) systems, three-dimensional (3D) structures can improve the functions of various electronic devices^{1–3}. For instance, high-aspect-ratio 3D architectures can enhance the capacity of batteries and improve the sensitivity of sensors by increasing the effective surface areas^{4,5}. It has also been shown that 3D circuits can integrate more components and achieve complex functions within a smaller size^{6,7}. To manufacture 3D structures, 3D printing has been applied in sensors^{8–11}, batteries^{12,13}, antennas^{14,15}, robotics^{10,16}, light-emitting diodes (LEDs)^{17,18} and thermoelectric modules¹⁹.

Direct ink writing (DIW) is a promising 3D printing technology that can be used to create high-resolution 3D architectures with simple printing processes and affordable equipment²⁰. Moreover, DIW is compatible with diverse functional materials with a wide range of viscosity, as well as colloidal inks containing solid microparticles²¹. However, because most printable materials used for DIW do not solidify immediately after printing, high-aspect-ratio free-standing 3D structures must be printed with support materials. Additionally, conventional printable inks are typically too viscous to achieve a high flow rate even when high pressure is applied, which limits the printing speed.

¹Department of Materials Science and Engineering, National University of Singapore, Singapore, Singapore. ²Department of Mechanical Engineering, National University of Singapore, Singapore, Singapore. ³Tsinghua-Berkeley Shenzhen Institute & Center of Double Helix, Tsinghua Shenzhen International Graduate School, Tsinghua University, Beijing, China. ⁴Institute for Health Innovation and Technology, National University of Singapore, Singapore, Singapore. ⁵Department of Electrical and Computer Engineering, National University of Singapore, Singapore, Singapore. ⁶Institute of High Performance Computing, Agency for Science Technology and Research (A*STAR), Singapore, Singapore. ⁷Department of Chemical and Biomolecular Engineering, North Carolina State University, Raleigh, NC, USA. ⁸The N.1 Institute for Health, National University of Singapore, Singapore, Singapore. ⁹These authors contributed equally: Shaohua Ling, Xi Tian. ✉e-mail: johnho@nus.edu.sg; benjamin.tee@nus.edu.sg

The key to make high-performance electronic devices is to develop printable materials with high electrical conductivity²². Conductive polymers such as ionic hydrogels are promising materials for making printable wearable devices due to their stretchability, transparency and biocompatibility^{9,23}, but their low conductivity restricts electrical functions. Printable inks based on poly(3,4-ethylenedioxythiophene): polystyrene sulfonate have shown conductivity of over 100 S cm^{-1} (refs. 24,25). Moreover, printable inks based on silver nanoparticles/flakes can achieve high conductivity of over $1 \times 10^5\text{ S cm}^{-1}$ (refs. 14,26,27), and have been used to print tactile sensors²⁸, microelectrodes²⁹ and radio-frequency electronics¹⁴. However, printed silver inks may require post-treatments, such as laser sintering and high-temperature annealing, to improve conductivity.

Liquid metals, such as eutectic gallium–indium (eGaIn), are another kind of printable ink with metallic conductivity^{30–32}. They are liquid and soft at room temperature and thus excellent candidates for printed stretchable electronics, but their intrinsic softness hinders creating self-supporting 3D functional structures. Alternatively, Field’s metal—a eutectic alloy of 51.0 wt% indium, 32.5 wt% bismuth and 16.5 wt% tin—is an ideal material for 3D printing, since it has a conductivity of $2 \times 10^4\text{ S cm}^{-1}$, a low melting point of 62°C and low toxicity³³. An electric-field-assisted DIW approach has been developed to create 3D architectures out of Field’s metal with high resolution through layer-by-layer stacking³⁴, and an electrohydrodynamic printing method has been used to create Field’s-metal-based stretchable circuits³⁵. However, free-form printing of free-standing 3D solid metallic structures has not yet been achieved.

In this Article, we report a 3D printing technique to create free-standing metal structures with Field’s metal. The driving force for the Field’s metal is shear in planar 2D writing and tension in out-of-plane 3D printing. When external pressure is used to force molten Field’s metal out of the nozzle, it causes rupturing of the oxide skin and beading of the printed wire. Using the tension-driven method without external pressure, uniform and smooth metal wires with tunable line widths from 100 to $300\text{ }\mu\text{m}$ can be printed with speeds of up to 100 mm s^{-1} . Moreover, due to the rapid solidification of Field’s metal at room temperature, we can create out-of-plane metal filaments at slope angles between 90° (vertical) and 0° (horizontal) without supports.

We use the approach to create different free-standing 3D metal structures, including standing letters, a cubic framework and scalable helical structures. These 3D architectures achieve excellent structural retention, aspect ratios of up to 750:1, electrical conductivity of $2 \times 10^4\text{ S cm}^{-1}$ and self-healing capability. The technique is compatible with various soft and stiff substrates. To investigate the mechanism of this method, we analyse the thermal physics in free-standing printing. In addition, to illustrate the wider potential of the approach, we print a wearable multilayer 3D circuit for battery-free temperature sensing and free-standing hemispherical helical antennas for wireless non-contact vital sign monitoring. Compared with conventional 2D spiral antennas, these have a smaller form factor, better directivity and enhanced sensitivity. We also fabricate 3D electromagnetic bandgap (EBG) metamaterials, which can suppress undesirable electromagnetic interactions and enhance the performance of antenna arrays.

Tension-driven conductive high-aspect-ratio metal 3D printing of Field’s metal

As shown in Fig. 1a, the printing system used for conductive high-aspect-ratio metal 3D printing (CHARM3D) is composed of a commercial print head with an integrated heater and a four-axis micro-positioning stage, which is able to move in the x , y and z axes and rotate in the x – y plane according to a 3D predesign. In general, pressure sources such as pneumatic pressure controllers or mechanical pumps are one of the essential components for 3D printers to drive DIW. However, in our case, the ink barrel is open to air instead of connecting with a pressure supplier. There is no external pressure needed during the whole 3D

printing process. Such pressure-free technique eliminates the need for bulky pumps and pressure controllers, which greatly simplifies the 3D printer.

Molten Field’s metal has a large surface tension of around 410 mN m^{-1} at 108°C and a low viscosity of about 27 mPa s at 80°C (refs. 35,36). Due to its high surface tension and low viscosity, pressure-driven DIW could not produce uniform metal wires on a substrate. Instead, a series of small beads were always observed to arise on printed metal wires before solidifying (Fig. 1b). The reason for this beading issue has been revealed (Supplementary Fig. 1)³⁷. The pressure applied to molten Field’s metal is uniformly distributed within the whole liquid volume, including the printed metal wire as long as it connects with the nozzle and is in the liquid phase. The pressure inside the printed wire is higher than the yield stress of the thin oxide layer, which forms instantaneously when exposed to air. Thus, the oxide skin ruptures and the low viscosity allows molten metal to flow out readily and to bead up due to its large surface tension. The pressure applied to the ‘ink’ barrel is the main cause of undesired beading.

To address this issue, we do not apply external pressure and instead drive CHARM3D by shear for the planar 2D ink writing and by tension for the out-of-plane 3D printing. The tension arises from the liquid bridge that spans from the molten metal in the nozzle and the leading edge of the solid, printed part. Compared with pressure-driven DIW (Fig. 1b), tension-driven CHARM3D can print continuous, uniform and smooth metal wires under the same conditions (Fig. 1c), as the oxide skin is stable in the absence of pressure and prevents printed metal ink from beading.

To initiate, the entire steel nozzle tube must be fully filled and wetted with molten metal before the first printing, which could be achieved by pressing down the syringe head cap to extrude out a small amount of molten metal ink through the nozzle (Supplementary Fig. 2). Once initiated, the nozzle tube will be wetted all the time even when the metal ink runs out in the barrel, and the nozzle can be reused for more than one month without any sign of corrosion or clogging. After initiation, there should be a small amount of residue metal remaining on the nozzle tip. They are usually found as a cone (Supplementary Fig. 3), instead of a typical meniscus in conventional DIW. The residual cone on the nozzle tip is the sign of successful initiation. The head cap will be removed after initiation and the top end of the ‘ink’ barrel will be open to air during printing.

To print metal patterns, when the nozzle tip is in close proximity to the substrate, the residue metal cone touches and adheres to the substrate. Then, the relative parallel motion between nozzle and substrate induces shear to continuously pull-out molten metal from the nozzle owing to its low viscosity. During printing, the steel stage that supports the substrate efficiently disperses heat and makes the printed metal patterns solidify immediately. To terminate the printed structure, a high speed of over 30 mm s^{-1} is applied in the z -axis direction to break the ink flow by lifting the print head. After printing, there is always a residual metal cone remaining on the nozzle tip for initiating the next printing process. If the metal ink runs out, DIW can be carried on after re-adding metal into the ink barrel without an initiation step. Moreover, the printed metal can be recycled as the Field’s metal does not react with the substrates used in this work and printed metal structures can be peeled off from the substrates without leaving a residue.

For out-of-plane 3D printing, the situation is similar to planar writing. The extruded metal ink from pressure-driven DIW always becomes droplets at the nozzle tip rather than a uniform metal filament, as the excessive pressure in molten metal continuously ruptures the thin oxide skin and pushes out molten metal to form a droplet until it falls. This issue has been eliminated by removing the external pressure source. Like planar printing, to create out-of-plane 3D metal structures, the residual cone on the nozzle tip must first touch and adhere to the substrate. Then, the tension generated when the nozzle moves away from the substrate (moving in the z axis) can smoothly pull-out molten

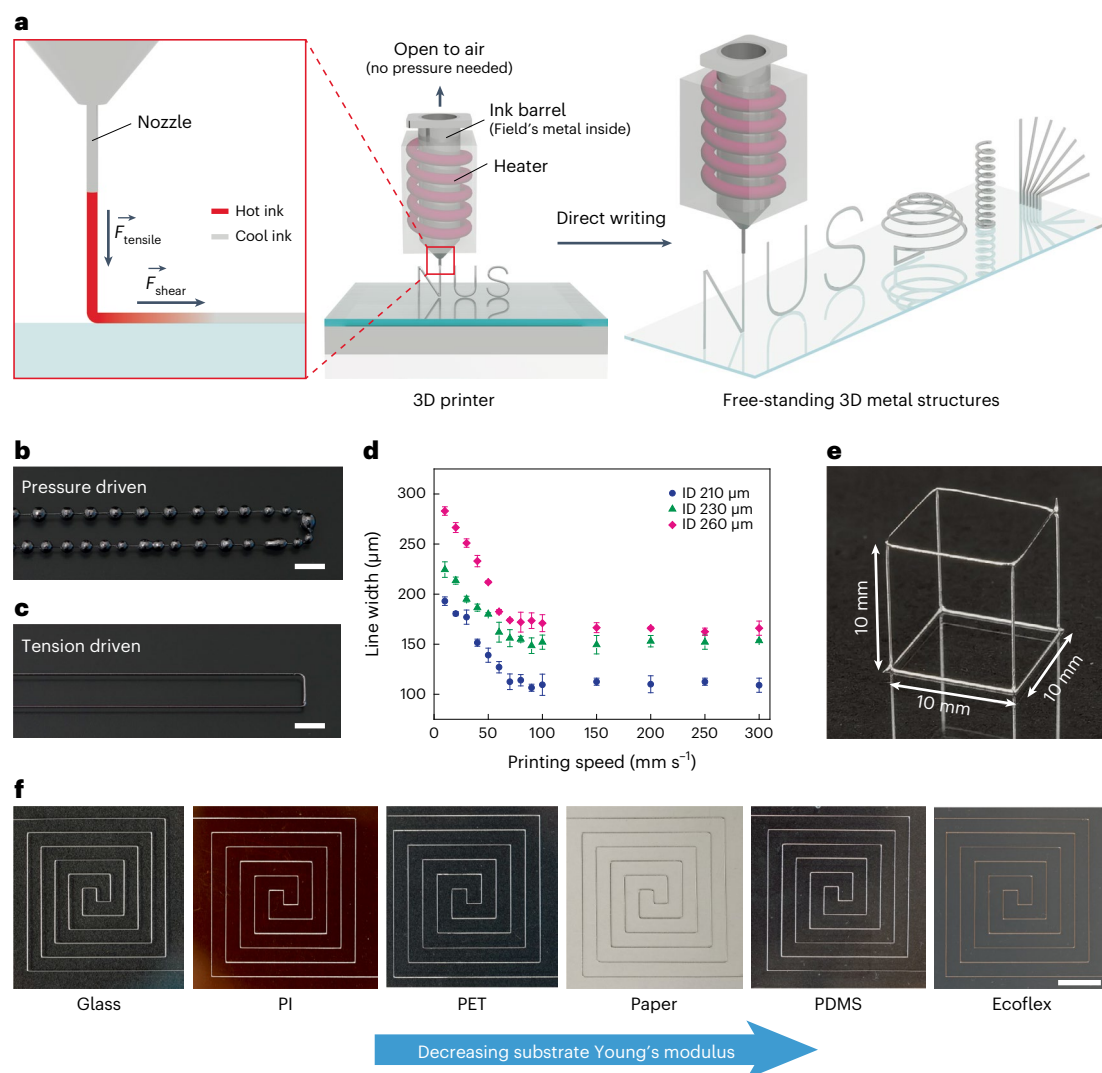


Fig. 1 | Conductive high-aspect-ratio 3D printing of Field's metal.

a, Schematic of the tension-driven CHARM3D method for free-standing 3D metal architectures. **b, c**, Photographs of metal wires printed by pressure-driven ink writing (**b**) and tension-driven ink writing (**c**) under the same conditions. Scale bars, 3 mm. **d**, Plot of the line width of printed metal wires versus the printing

speed with different IDs of nozzles at 80 °C. Data are presented as mean values \pm standard deviation ($n = 5$). **e**, Photograph of a printed free-standing 3D cubic framework. **f**, Photographs of metal patterns printed on different substrates, including (from left to right) glass, polyimide (PI), polyethylene terephthalate (PET), office paper, PDMS and Ecoflex. Scale bars, 5 mm.

metal to create free-standing 3D metal structures. Once it leaves the nozzle tip, printed metal filaments cool down and solidify immediately to support subsequent ink, and thus, no external support is required during the whole 3D printing process.

Printing free-standing 3D structures without support is a bottleneck for conventional DIWs, since the inks do not solidify immediately after printing. However, using our method, free-standing and even overhanging 3D structures can be created. For example, we demonstrate a free-standing 3D metal cubic framework printed by CHARM3D (Fig. 1e), where it would be impossible to print the overhanging top square framework without supports using conventional DIWs. On printing, the 3D structures are rigid, stable and highly conductive, so they could be applied in various electronic devices without any post-treatments.

To investigate the planar 2D printability of CHARM3D, a series of parameters such as printing resolution, nozzle inner diameter (ID), print-head temperature and travelling speed (printing speed) were systematically studied (Fig. 1d and Supplementary Fig. 4). A polydimethylsiloxane (PDMS) film was chosen as the substrate and the distance between the nozzle tip and substrate was fixed at 100 μm during

every printing. As shown in Fig. 1d, the line width of the printed metal wires is tunable between 100 and 300 μm . In the low-printing-speed range (10–20 mm s^{-1}), line widths are close to the nozzle IDs. Line widths reduce as the printing speed increases for a certain nozzle ID and temperature and then remain constant after the printing speed exceeds 100 mm s^{-1} . However, the metal may solidify and clog the nozzle if the printing speed is lower than 10 mm s^{-1} since the small flow rate of hot ink and fast heat dissipation of the steel stage below cause the temperature at the nozzle tip to drop too fast. When the printing speed is higher than 100 mm s^{-1} , the printer vibrates, which may be detrimental to the printing system. Thus, the speed range for stable and reliable printing is between 10 and 100 mm s^{-1} . Moreover, line widths increase at a certain printing speed as the nozzle ID increases from 210 to 260 μm . However, the nozzle ID could not exceed 260 μm ; otherwise, the molten metal would flow out uncontrollably, as the resistance when the ink flows through a large nozzle tube is not enough to overcome gravity. If the nozzle ID is smaller than 210 μm , it is difficult to print continuous metal wires, since the resistance in a narrow nozzle is too large to be overcome by tension and gravity. On the other hand, the print-head temperature also has an impact on the printing resolution

because it determines the viscosity of molten metal ink. For a given nozzle ID and printing speed, the line width may increase a bit as the print-head temperature increases from 80 to 100 °C due to reduced ink viscosity (Fig. 1d and Supplementary Fig. 4). It is worth mentioning that our printing speed is one order of magnitude higher than that of previously reported DIWs. Usually, the printing speed of traditional DIWs is smaller than 10 mm s⁻¹, as typical conductive inks such as silver pastes have a high viscosity, which restricts the flow rate even under a high pressure. However, the low viscosity of molten Field's metal and instantaneous formation of oxide skin enable fast printing. Optical microscopy images (Supplementary Fig. 5) show that printed metal wires have excellent uniformity, smooth surface and metallic lustre regardless of the nozzle ID, print-head temperature and printing speed. All the printed metal wires exhibit excellent consistency in line width with a standard deviation of smaller than 5 µm (Supplementary Fig. 6).

Using CHARM3D, various planar metal patterns could be created with high quality and high efficiency, such as a 2D inductor (Supplementary Fig. 7). The printed metal features exhibit high electrical conductivity, and the thin oxide layer does not affect the electrical performance; therefore, no post-treatment is needed. The metal patterns could be reliably printed on diverse substrates with a wide range of Young's modulus, from rigid glass to soft PDMS and Ecoflex (Fig. 1f). Moreover, the surface roughness of substrates seems to have no major impact, as metal patterns could be printed on rough surfaces like paper. The substrate compatibility enables potential applications in fabricating both soft and rigid devices. Furthermore, there is no surface pretreatment required for the substrates utilized in this work, except for basic cleaning. However, it has been reported that some surface treatments such as ultraviolet–ozone and oxygen plasma could modify the surface chemistry and further enhance interfacial adhesion between substrates and printed metal features³⁷.

Printing free-standing 3D structures

Creating complex out-of-plane 3D structures is an important capability for 3D printing. Here we primarily construct 3D structures by a layer-by-layer deposition of metal filaments. We illustrate this by printing a series of out-of-plane metal structures with 30 layers (Fig. 2a). For each structure, all the 30 layers bond to form a single entity rather than separate filaments, because hot metal ink re-melts the top volume of the underlying layer and fuses together during stacked printing. This feature enables printed layers to become a solid and stable foundation for subsequent layers, thereby making it possible to create tall and complex structures without deviation or collapse. To illustrate this superiority, two hollow cylinders with variational radii have been printed (Fig. 2a, middle). The variation in radius shrinkage and expansion is 90 µm for every layer, where the line width is 200 µm, showing that the whole structures are still printable and stable even if nearly half of every metal filament is overhanging. In addition, two twisted cubes have been created by rotating the *x*–*y* plane after each layer printing with a magnitude of 1° and 2° (Fig. 2a, right). We note that layer-by-layer deposition can only construct a limited variety of 3D structures, but it is the only strategy to adapt DIW to create 3D architectures.

To further exploit the potential to create sophisticated and functional out-of-plane structures, a series of metal filaments with various slope angles (Fig. 2b–e) were pulled from the nozzle by tension when the nozzle was retracting at the corresponding slope angles after adhering the residual cone on the substrate (Supplementary Video 1). They are able to stand steadily without supports, even at slope angles lower than 45°, unlike for conventional DIWs. Those filaments are uniform and smooth with excellent structural retention for all the printed slope angles. The line widths (diameters) of free-standing filaments are mostly determined by the nozzle size when slope angles are higher than 60°, and they reduce slightly as the slope angles diminish (Fig. 2f and Supplementary Fig. 8). The length of the free-standing filaments is scalable from millimetres to decimetres and the longest single

free-standing filament that could be printed is around 150 mm due to the limited moving range of the stage and print head (Supplementary Fig. 9). It is possible to print longer free-standing filaments as the solidified metal is rigid, but gravity may lead to undesired deformation (Supplementary Fig. 9a). The print-head temperature does not greatly affect their widths. To achieve smooth printing, the speed for free-standing printing should be lower than 1 mm s⁻¹, because heat dissipation lessens substantially once the printed structure is no longer in contact with the substrate. Thus, the printed metal in the free-standing structures takes more time to cool and solidify.

Such effective and precise free-standing printing capability enables the free-form creation of sophisticated 3D metal structures. To illustrate this, we printed three free-standing letters of 'NUS' with a height of around 6 mm (Fig. 2g and Supplementary Video 1). Although they were printed at 75 °C using two or three steps, each letter is mechanically continuous and can be lifted from one point (Supplementary Fig. 10). We also print a free-standing cubic framework with a side length of 1 cm (Fig. 1e and Supplementary Video 1). Horizontally printing overhanging structures such as the square framework on the top of a cube is challenging for conventional DIW. Here a smooth and uniform metal filament square can be printed on top of the cubic framework with high precision. At each vertex, the print head is programmed to deposit metal ink exactly on the top tip of every vertically standing filament. Solid adhesion is achieved at every vertex to support and stabilize the whole architecture as the just-printed metal ink is hot enough to re-melt a small volume of solidified metal on the vertical filament top. To visualize this, we conducted a numerical analysis to simulate the heat transfer around the vertex during the connection process. As a result, 0.9-mm-long vertical filaments can be re-melted at the top by the hot horizontal filament after it flits across the vertex (Supplementary Fig. 11 and Supplementary Video 7). The liquid part will fuse together and realize robust connection at the vertex.

Furthermore, the capability of rotating the stage in the *x*–*y* plane enables printing circular- and spiral-based 2D and 3D structures with high precision. To illustrate this, a series of free-standing helixes with various dimensions have been printed by coordinating the stage rotation in the *x*–*y* plane as the print head retracts along the *z* axis (Fig. 2h, Supplementary Fig. 12 and Supplementary Video 2). The diameters of these printed helical structures are scalable from micrometres to millimetres, with the smallest pitch of around 600 µm. If the diameter is higher than 5 mm, the bottom parts may deform due to gravity. During tensile testing, the printed helical structures exhibit elastic and plastic behaviour (Supplementary Fig. 13). Their spring mechanical properties and high electrical conductivity enable printed helixes to be a candidate for stretchable conductors. In addition, a series of free-standing hemispherical helical structures with variable diameters from 4 to 6 mm have been produced (Fig. 2i). The whole hemispherical helix is supported by a single short vertical filament. Such hemispherical helixes could be applied as 3D antennas, and their performance is explored in the following section. Although conventional DIWs typically require post-treatment to realize the desired electrical properties such as annealing or laser sintering, which can cause volume shrinkage in printed 3D structures, the 3D structures printed using our method do not require any post-treatment and thus show good structural retention.

Highly conductive and high-aspect-ratio printed 3D structures are useful for creating complex components integrated in a small volume. However, inks developed for conventional DIWs cannot easily achieve free-standing filaments with high aspect ratios. Conductive-polymer-based inks and graphene-based inks exhibit relatively low electrical conductivity (Fig. 2j and Supplementary Table 1). Liquid-metal-based inks and silver-nanoparticle-/silver-flake-based inks can realize sufficient conductivity, but they are unable to solidify on printing, either because they are intrinsically liquid (liquid metal) or require post-treatment to accelerate their solidification (silver paste). Thus, it is difficult for those inks to become self-supported

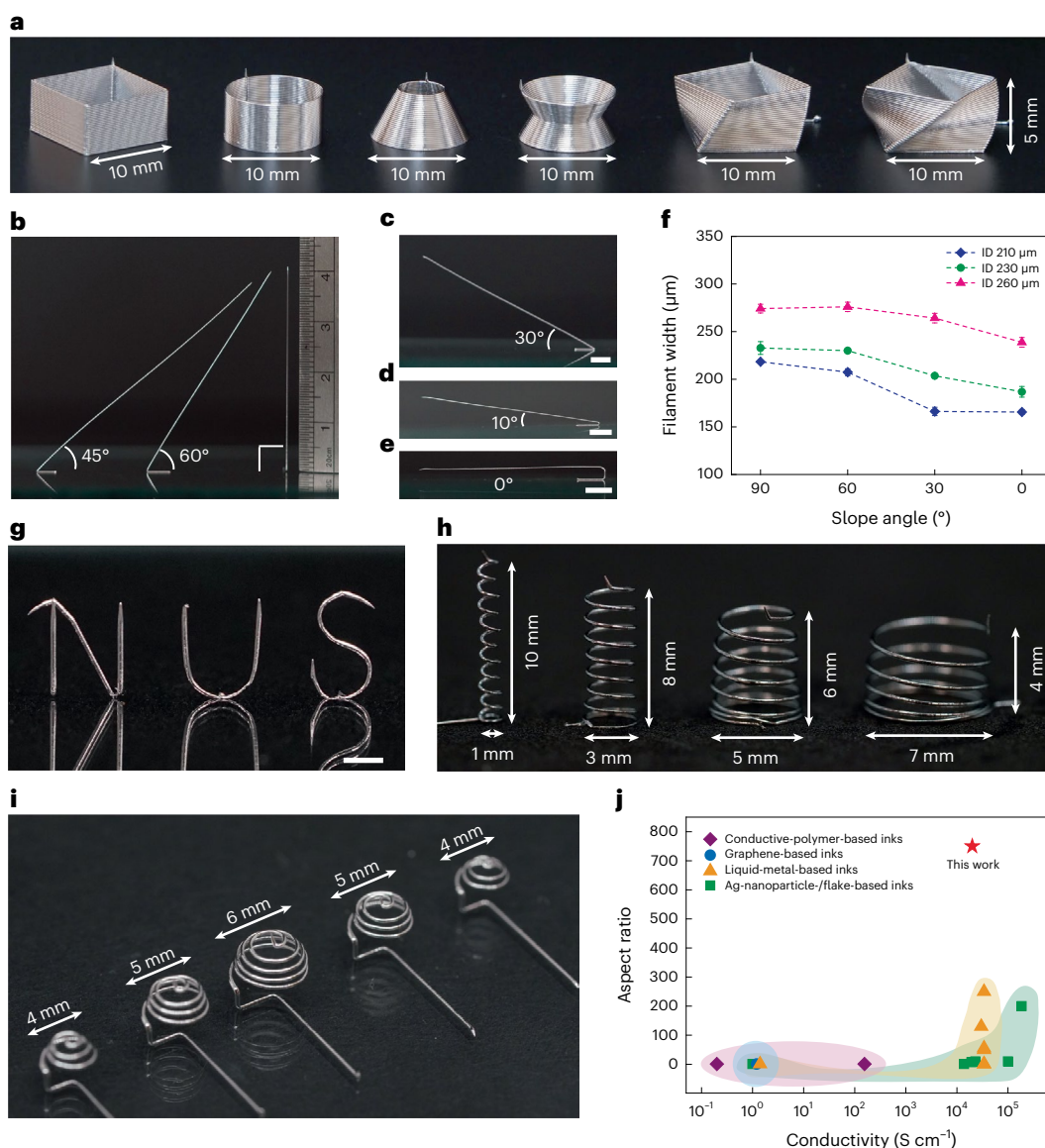


Fig. 2 | CHARM3D of free-standing 3D metal structures. **a**, Photograph of an out-of-plane 3D architecture array built by the layer-by-layer deposition of Field's metal. **b–e**, Photographs of printed free-standing metal filaments with slope angles of 90° (vertical), 60° and 45° (**b**); 30° (**c**); 10° (**d**); and 0° (horizontal; **e**). Scale bars, 5 mm. **f**, Plot of the width of printed free-standing metal filaments versus the slope angles with different IDs of nozzles at 80 °C. Data are presented as mean values \pm standard deviation ($n = 5$). **g**, Photograph of the printed

free-standing letters of 'NUS'. Scale bars, 3 mm. **h**, Photograph of the printed free-standing helical metal structures with diameters of 1, 3, 5 and 7 mm (from left to right). **i**, Photograph of a printed free-standing hemispherical helix array with diameters of 4, 5, 6, 5 and 4 mm (from left to right). **j**, Comparison of the conductivity and aspect ratio of reported 3D printed conductors made by DIW with this work.

high-aspect-ratio 3D structures. Using Field's metal, the printed free-standing 3D metal structures can exhibit high electrical conductivity and high aspect ratio. The highest aspect ratio achieved with a 150-mm-long free-standing filament was 750:1.

Tension-driven printing could be generalized to a broad range of metallic materials, including ordinary metals (such as aluminium-based alloys and steels) and low-melting-temperature alloys (for example, gallium, Wood's metal and Rose's metal) if they fulfil three criteria. First, the molten metals must have similar low viscosity as Field's metal ($\sim 27 \text{ mPa s}$ at 80 °C)³⁶; therefore, it can be pulled out through the nozzle by small tension. For different printing setups, the viscosity range for successful printing can be determined by the formula derived in the 'Viscosity Thresholds for Tension-Driven 3D Printing' section in the Supplementary Information. Second, oxidation must occur immediately on the surface of the just-printed metals such that the solid oxide layer

can overcome the surface tension to prevent beads forming before solidifying, and thus, uniform and smooth filaments are formed. Third, 3D printable metals should be solid at room temperature so they can quickly solidify after printing to sustain free-standing 3D structures.

Thermal physics of CHARM3D

We studied the thermal physics in the process of 3D printing through finite-element analysis (FEA). The heat transfer model for the simulation is provided in the Supplementary Information. The heat transfer characteristics are mainly determined by the nozzle temperature T and printing speed v . Figure 3a shows the FEA results of the temperature distribution in the free-standing filament and helical structure during bottom-up printing. Three parameters—liquid length, liquid arc length and liquid angle—quantify the liquid volume in the just-printed structures, where the temperature is still higher than the melting

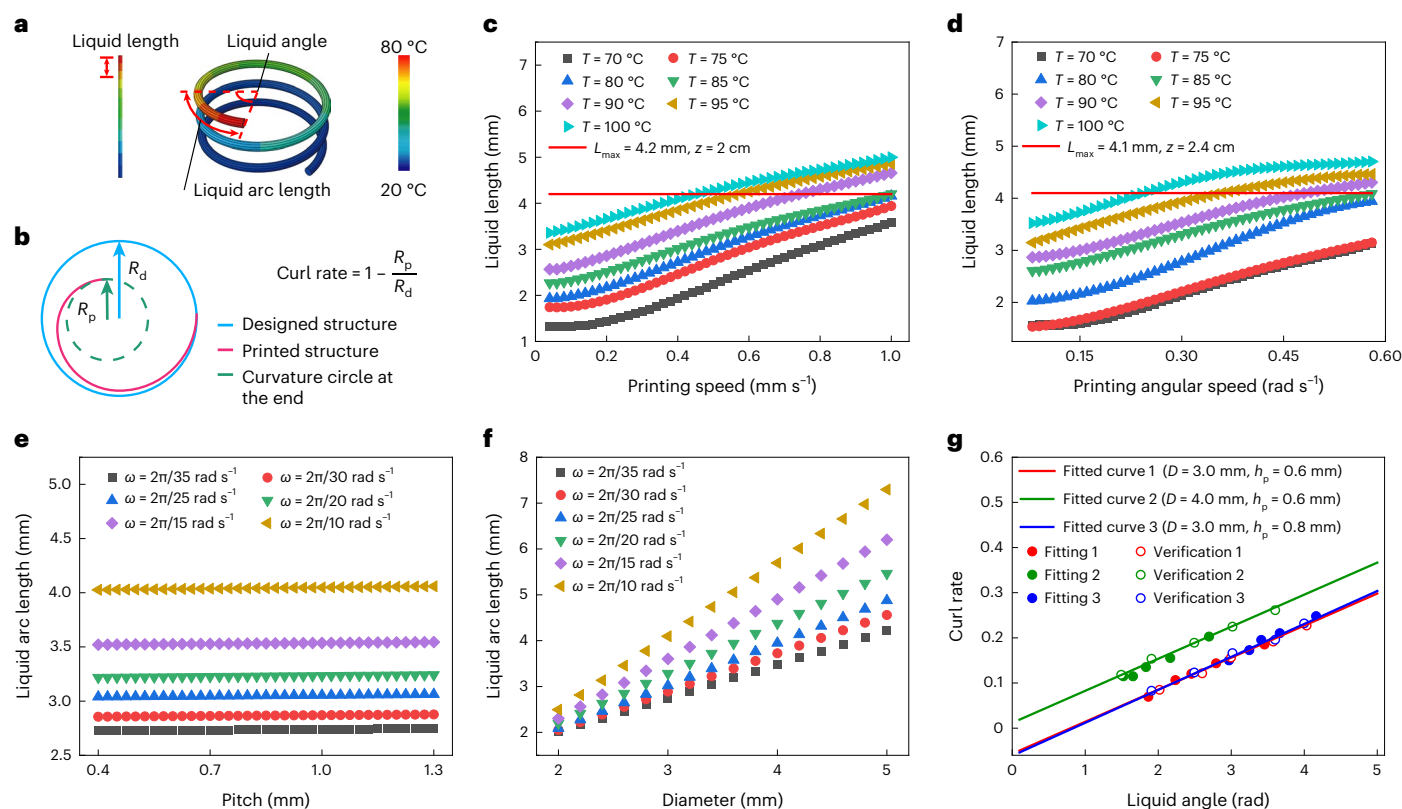


Fig. 3 | Numerical analysis of thermal and mechanical physics during printing. **a**, Schematic of the temperature distribution when printing vertical filaments and helical structures. **b**, Schematic of the structural deviation from top view when printing helical structures. **c**, Liquid length variation during printing vertical filaments with different speeds at 70–100 °C. The maximum liquid length (L_{\max}) without bulging is 4.2 mm if the height of the molten metal volume (z) in the syringe is 2 cm. **d**, Liquid arc length variation during printing

helical structures with different speeds at 70–100 °C. The maximum liquid arc length (L_{\max}) without bulging is 4.1 mm if the height of the molten metal volume (z) in the syringe is 2.4 cm. **e, f**, Liquid arc length variation when printing helical structures with different pitches (**e**) and diameters (**f**) at 80 °C. **g**, Relationship between liquid angle (from FEA) and curl rate (from experiment) for printing helical structures with different diameters (D) and pitches (h_p).

point. The liquid volume may lead to bulging during the printing of free-standing filaments, causing structural collapse. To reveal the relationship between the liquid length, nozzle temperature and printing speed, we simulate the heat transfer during the free-standing printing of vertical filaments. As shown in Fig. 3c, high nozzle temperatures always result in long liquid lengths in the printed filaments. Moreover, the liquid length will gradually elongate as the printing speed increases. According to the mechanical analysis (Supplementary Information), the liquid volume of the molten Field's metal applies an inner pressure on the oxide skin, leading to circumferential stress on the oxide shell. There is a critical liquid length of around 4.2 mm when the height of the molten metal volume in the syringe is 2.0 cm, where the circumferential stress equals the yield stress of the oxide skin. If the liquid length is longer than 4.2 mm, the liquid portion in the filament will bulge uncontrollably. Thus, to avoid the bulging issue, the printing speed should be smaller than 1 mm s^{-1} at 80 °C. In experiments, bulging was found to frequently occur if the printing speed is higher than 1 mm s^{-1} , in agreement with the FEA analysis.

For helical structures, the liquid volume may lead to deviation in the printed structures from the predesign, affecting the structural retention. As illustrated in Fig. 3b, the shrinking radius of the printed helical structure deviates from the designed structure during printing because the liquid volume is pulled to be straight under tension. R_d and R_p are the radii of the designed helical structure and the curvature circle at the top end of the printed structure, respectively. The curl rate is defined to quantify the structural deviation in the printed helix from the predesign. To identify the influence factors on the liquid arc length,

we systematically analyse the heat transfer during printing under different parameters, such as nozzle temperature, printing angular speed, diameter and pitch of helical structures. Figure 3d shows that the liquid arc length increases when the nozzle temperature and printing angular speeds increases. However, the FEA results for printing at nozzle temperatures of 70 and 75 °C are almost the same. The similar liquid arc lengths may imply that the printed inks solidify quickly under these conditions as these nozzle temperatures are very close to the melting point of Field's metal. In the practice printing experiment, we found that the printed filaments were easy to break as the ink solidified at the nozzle tip and clogged the nozzle if the nozzle temperature was lower than 80 °C. Thus, 80 °C is the optimal nozzle temperature for printing helical structures with the smallest structural deviation. There is also a critical liquid arc length of around 4.1 mm for the bulging issue, when the height of the molten metal volume in the syringe is 2.4 cm.

Furthermore, Fig. 3e, f exhibits the effect of varying the pitch and diameter, respectively, of helical structures on the structural deviation when the nozzle temperature is fixed at 80 °C. For a given diameter, the change in pitch will not greatly affect the liquid arc length regardless of the printing angular speed, if the pitch is smaller than the diameter. On the other hand, for a certain pitch, increasing the diameter of helical structures will elongate the liquid arc length and thus impact the structural retention. High printing angular speeds can also aggravate the structural deviation. Finally, to predict the structural deviation in the free-standing printing of helical structures, we study the relationship between the liquid angle and curl rate (Fig. 3g). The liquid angle is obtained by FEA, whereas the

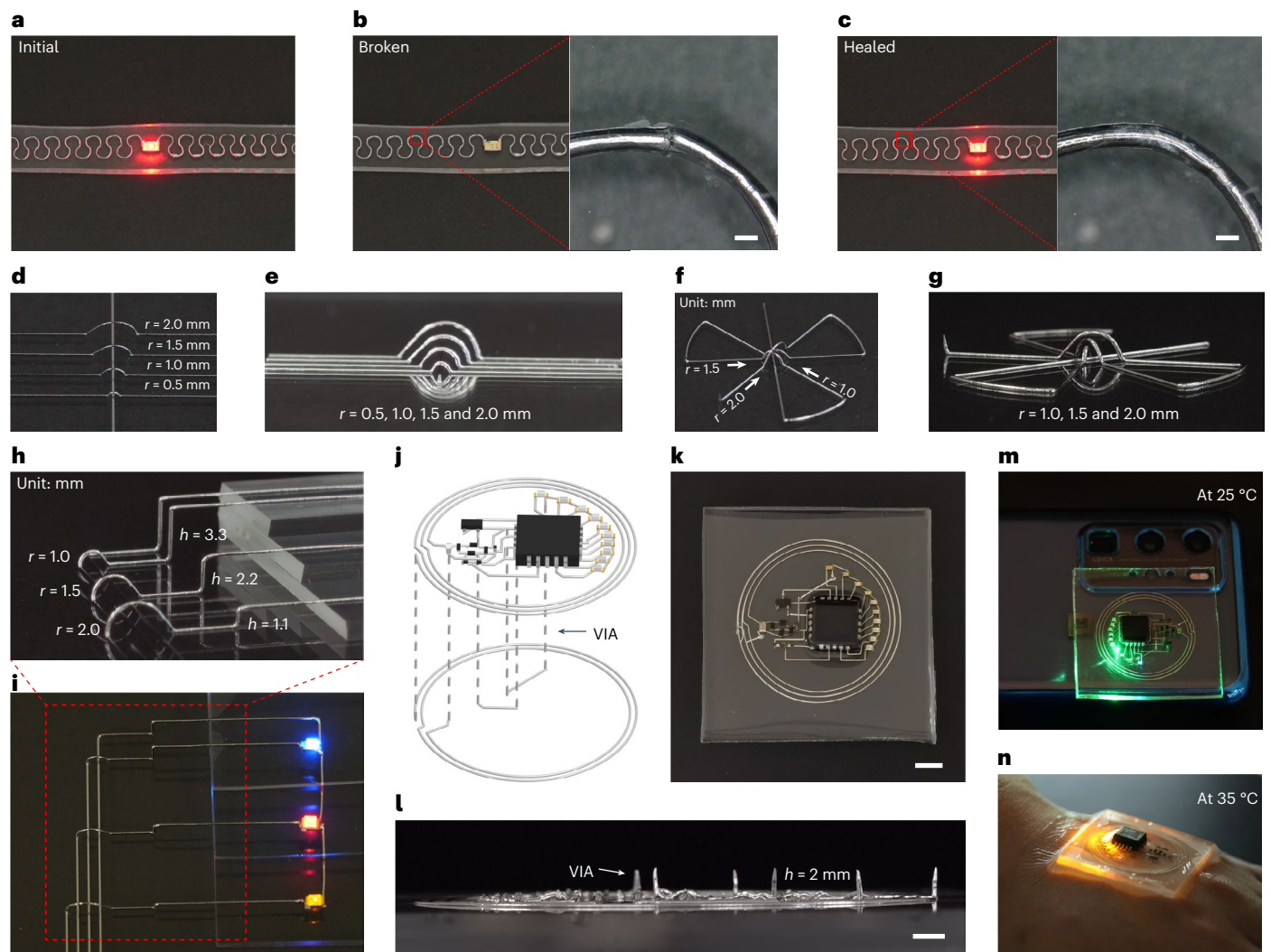


Fig. 4 | Printed self-healing and 3D electronics. **a–c**, Photographs of a printed circuit initially (**a**), when broken (**b**) and after self-healing with mild heat treatment (**c**). The insets show photographs of the broken point before (**b**, right) and after (**c**, right) self-healing, as obtained from an optical microscope. Scale bars, 200 μm . **d,e**, Photographs of printed arc bridges with different radii (r) as viewed from the top (**d**) and front (**e**). **f,g**, Photographs of printed multiple arc bridges with diverse radii (r) crossing over the same point from the top view (**f**)

and front view (**g**). **h,i**, Photographs of a printed 3D circuit with VIAs connecting four layers at varying heights (h) from the side view (**h**) and top view (**i**). **j,k**, Schematic (**j**) and photograph (**k**) of a 3D printed multilayer circuit for the battery-free temperature sensor. Scale bar, 5 mm. **l**, Side view of the printed VIAs with a height (h) of 2 mm on the top-layer circuit. **m**, Photograph of the printed circuit powered by a phone via NFC at 25 $^{\circ}\text{C}$. **n**, Photograph of the printed circuit worn on a human hand at 35 $^{\circ}\text{C}$.

curl rate is obtained by experiment. For a certain set of diameters and pitches, we establish a linear relationship between the liquid angle and curl rate by fitting the known data. The linear function can be used to predict the structural deviation for any printing conditions. The validation data show good alignment with the linear relationship, and thus, the linear function is reliable to control the diameter shrinkage during printing.

Printed self-healing and 3D electronics

Self-healing capability enables devices to automatically recover from mechanical damage. This could extend the lifetime and reduce the cost for wearable electronics that are easy to wear or disrupt during daily use. Printed metal circuits have such a self-healing capability owing to the low melting point of Field's metal. To illustrate this, a circuit was fabricated by printing serpentine wires to connect a red LED and encapsulating them with PDMS (Fig. 4a). The LED was initially lit, but it lost power once a break occurred (Fig. 4b). When heated over 62 $^{\circ}\text{C}$ by a mild hot-air gun, Field's metal re-melted and the two ends beside the break point fused and re-joined together without an obvious scar

(Fig. 4c and Supplementary Video 3). After the self-healing process, the LED was able to light again.

A series of arc-shaped metal bridges were created to cross over 2D wires and 3D structures without physical contact. To find the optimal condition, the printing speed of arc bridges was studied, where the arc radius was designed at 2 mm (Supplementary Fig. 14). High-speed printing resulted in imperfect arc shapes due to insufficient cooling for free-standing parts, although they still could surpass the underlying wires without physical contact. Thus, the printing speed of 1 mm s^{-1} was chosen to create reliable arc structures. The radius of the arc bridges is tunable from submillimetre to millimetre scales to meet the different requirements of crossing span (Fig. 4d,e). A multiple-cross architecture was created consisting of three arc bridges with various radii of 1.0, 1.5 and 2.0 mm, respectively, crossing over the same point (Fig. 4f,g). Vertical interconnect accesses (VIAs) are used to connect layers when fabricating 3D circuits. However, previous strategies to make VIAs, such as laser ablating holes and filling with conductive materials, are complicated and time-consuming. We show that CHARM3D can address this difficulty by 3D printing VIAs with various heights that follow

overhanging wires. This was used to connect four layers into one 3D circuit (Fig. 4h,i). The height and slope angle of VIAs are tunable within 0–40 mm and 0°–90°, respectively, increasing the degree of freedom for circuit design.

To further illustrate the capability of fabricating complex circuits, a 3D circuit with two layers of a battery-free temperature sensor system was printed by CHARM3D (Fig. 4j,k). To fabricate it, first, all the components were embedded in PDMS, except for the pads required for the connection. Then, in-plane metal wires and out-of-plane VIAs were printed to create coils and to connect the exposed pads in accordance with the circuit design (Fig. 4l). Next, after encapsulating the printed in-plane wires, the second layer of coils and wires were printed to connect all the VIAs and to complete the circuit, and finally, the second layer was encapsulated with PDMS. A fabrication process flow for the complete system is shown in Supplementary Fig. 15. Owing to the low melting point of Field's metal, traditional soldering was replaced with a 10 s heat treatment after fabrication, where printed wires re-melted to enhance the adhesion on component pads and joined with VIAs to form solid connections. This printed multilayer device was wirelessly powered by a smartphone through near-field communication (NFC) (Fig. 4m). The temperature sensor could sense temperature change and accordingly determine the ON/OFF status of each LED. Temperature variation was displayed by lighting LEDs from green, yellow and orange to red with increasing temperature (Supplementary Video 4). The device could be worn on a human hand to detect environment temperature (Fig. 4n).

3D printed antennas

Our method can be used to print 3D antennas with high degrees of freedom to manipulate current distribution and polarization. As a demonstrative example, we printed a 5 GHz hemispherical helical antenna that exhibits a substantially reduced form factor compared with the conventional 2D spiral antenna (Fig. 5a). From the comparisons of the reflection spectrum (Fig. 5b) and normalized radiation pattern (Fig. 5c), this 3D helical antenna shows less reflection and better directivity (6 dB higher gain) compared with the 2D spiral, which are essential parameters related to the radiation performance. We applied these antennas in wireless vital sign monitoring based on the Doppler radar technique, which relies on the detection of phase shifts in radio-frequency waves transmitted towards and reflected from a moving object^{38,39} (Supplementary Video 5). As shown in Fig. 5d, antennas were placed on the edge of a table and the working frequency was set to 5 GHz. Full-wave simulations of the antenna transmitting in a computational body model show directive-wave transmission to the body surface (Fig. 5e). The phase of the reflected signal is the key to vital sign detection because it is modulated by the physical movements of the body surface due to the deformation of the heart and lung within each cardio-respiratory cycle³⁹. The spectra of the reflected signals obtained from the 3D helical antenna can reveal distinct respiratory peaks as well as subtle heartbeat signals. This is attributed to the high directivity of our 3D helical antenna, enabling the detection of subtle physiological variations associated with the heartbeat (Fig. 5f). To validate the accuracy of our wireless sensing system, we simultaneously measured a reference respiration and electrocardiogram (ECG) signal (MP46, BIOPAC Systems). Figure 5g,j shows the normalized respiration and heartbeat signals, respectively, simultaneously obtained from the

same reflected wireless signal, demonstrating good agreement with the gold-standard references. The respiration rate (RR) intervals measured from our 3D helical antenna have a strong positive linear correlation with the reference RR intervals with Pearson's correlation coefficient $r = 0.8776$, and the beat-to-beat (BB) interval measurement results also show a strong positive linear correlation with the ECG R-peak intervals with Pearson's correlation coefficient $r = 0.8776$ (Fig. 5h,k). Furthermore, to assess the agreement of our wireless sensing system with the gold standard, the Bland–Altman analysis was implemented (Fig. 5i,l)⁴⁰. The results show excellent agreement between our wireless vital sign monitoring system and the commercial referenced sensors. Finally, we demonstrated wireless vital sign monitoring on a healthy subject for 2 min using our 3D helical antenna (Fig. 5m).

3D printed metamaterials

Metamaterials leverage the precise arrangement of periodic subwavelength structures to create electromagnetic properties superior to those in natural materials⁴¹. Metamaterials have shown substantial promise in the field of electromagnetic engineering^{42–44}, but their widespread adoption has been limited by difficulties in manufacturing the intricate 3D unit cells that constitute the metamaterials, which can incur high costs and complexity using traditional methods⁴⁵. We show that tension-driven 3D printing can easily create an EBG metamaterial structure (Fig. 6a). This EBG metamaterial comprises periodic 3D unit cells (Fig. 6b). The simulated dispersion diagram (Fig. 6c) shows that this EBG metamaterial structure creates a stopband within a specified frequency range, where wave propagation through the structure is inhibited. As a practical demonstration, we integrated the EBG metamaterial into a patch-antenna array to mitigate mutual coupling effects (Fig. 6d–f). Through the full-wave simulations of wave propagation within the array, we observed that traditional-antenna arrays are susceptible to unwanted signals due to electromagnetic interactions, a phenomenon known as mutual coupling. In contrast, the EBG metamaterial effectively suppresses surface-wave propagation, thereby ensuring high isolation within the array without mutual coupling issues. The measurement results (Fig. 6f) indicate that the EBG metamaterial reduced the $|S_{21}|$ value by over 20 dB, signifying a reduction of more than 99% in the coupling current. This result demonstrates the efficacy of our 3D printed metamaterial in enhancing the performance of antenna arrays through the suppression of unwanted electromagnetic interactions.

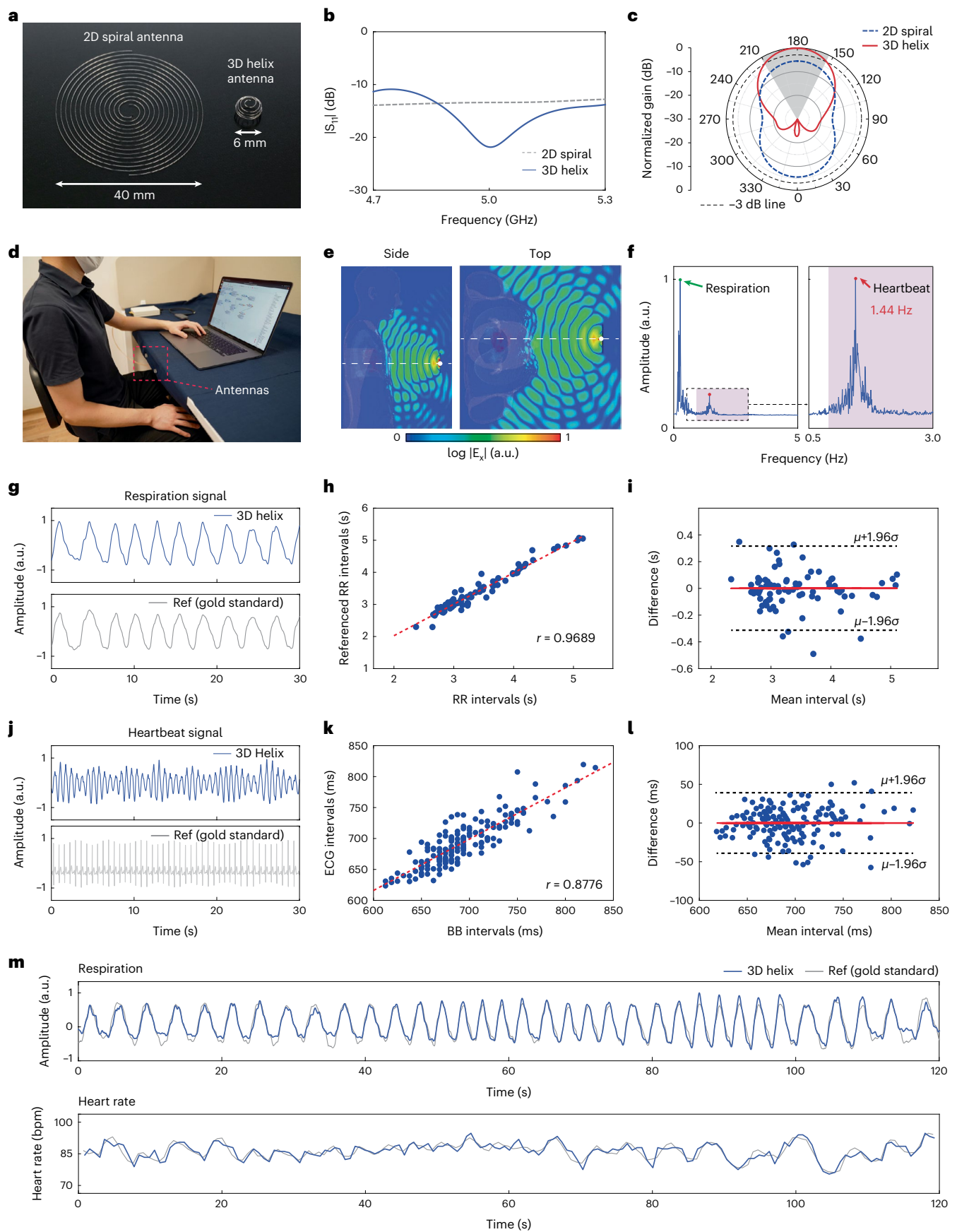
Conclusions

We have reported a technique to directly print free-standing 3D metal structures for electronics. Rather than relying on extrusion, our method uses tension to pull the metal ink from the nozzle to avoid the beading issue associated with extruding low-viscosity fluids. It can print uniform and smooth metal wires with a speed of up to 100 mm s^{−1} and on various substrates. In particular, using Field's metal, we are able to print free-standing metal filaments at slope angles ranging from 90° (vertical) to 0° (horizontal) without support, enabling the precise creation of various free-standing 3D metal structures without any post-treatments. All the printed 3D structures have high structural retention, electrical conductivity and aspect ratio of up to 750:1.

We performed systematic thermal physics analysis to understand the mechanism of printing and improve its precision. To demonstrate the versatility of CHARM3D, we fabricated complex 3D circuits with

Fig. 5 | 3D printed antenna for wireless vital sign monitoring. **a**, 3D printed hemispherical helical antenna compared with the conventional 2D spiral antenna. **b**, Reflection spectrum $|S_{11}|$ comparison. The 3D printed hemispherical helix shows less reflection. **c**, Normalized radiation pattern comparison. The gain is normalized to the overall highest value, which is 10.2 dBi. The 3D printed hemispherical helix has 6 dB higher gain. **d**, Wireless vital sign monitoring based on the Doppler radar technique. **e**, Full-wave simulations of wireless sensing in a computational human body model. The dashed lines show the cutting planes and

the white dots represent the helical antennas. **f**, Spectrum of the received wireless signal using a 3D helix antenna, showing respiration and heartbeat **g,j**, Measured vital sign waveforms of respiration (**g**) and heartbeat (**j**). **h,k**, Linear correlation between the 3D printed helical antenna and commercial sensors (gold standard) measured intervals. **i,l**, Bland–Altman plot showing the pairwise comparison. **m**, 2 min non-contact vital sign monitoring, demonstrating good agreement of the respiration waveform and heart rate with the gold-standard measurement.



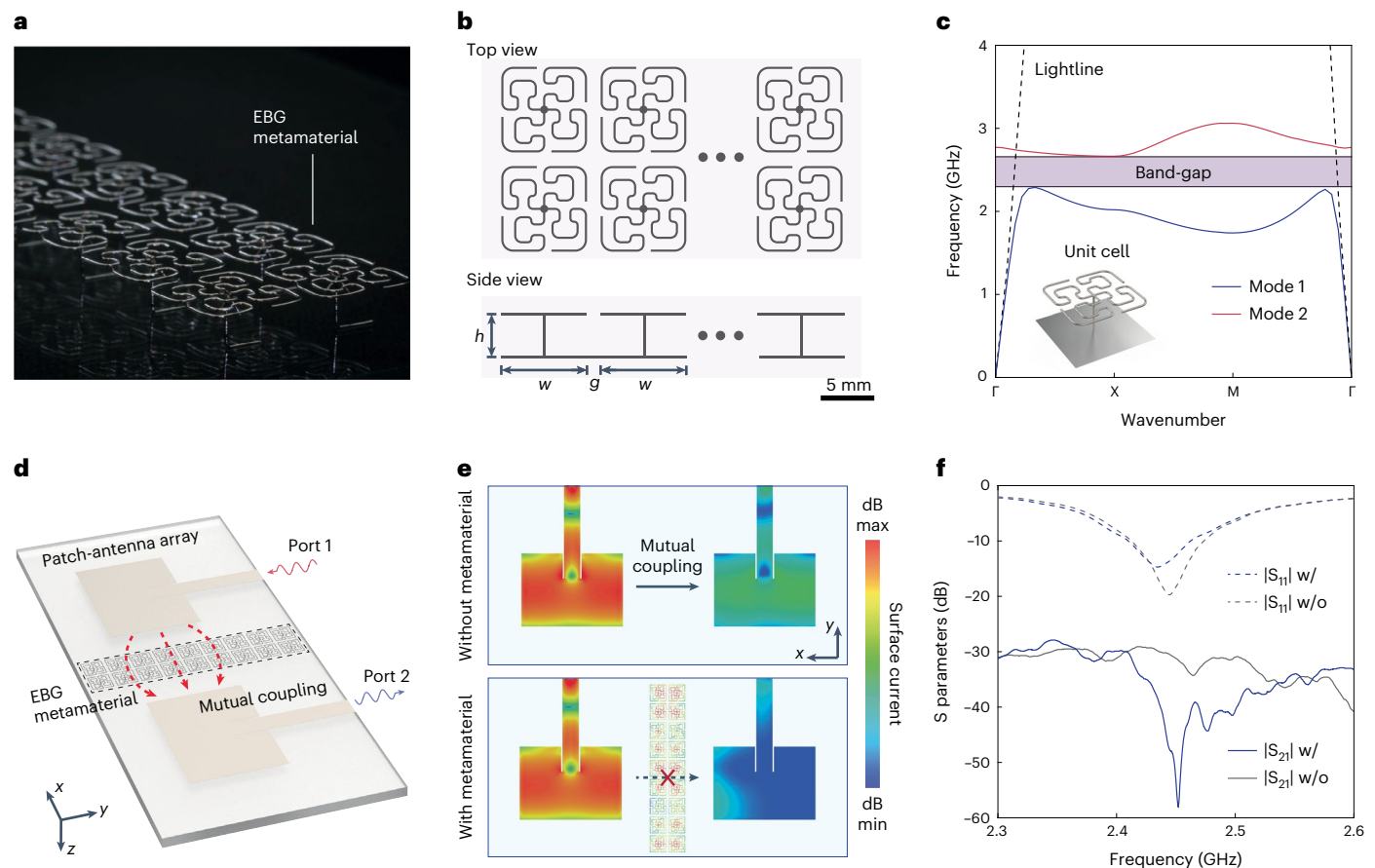


FIG. 6 | Free-standing 3D metamaterial. **a**, Image of the EBG metamaterial created by tension-driven 3D printing. **b**, EBG metamaterial structure and geometrical design parameters ($h = 4.000$ mm, $g = 1.275$ mm, $w = 8.000$ mm). **c**, Simulated dispersion diagram of the EBG metamaterial using CST MICROWAVE STUDIO. The vertical axis shows the frequency, and the horizontal axis represents the values of the wavenumbers in the Brillouin zone. **d**, Application of the EBG

metamaterial for reducing mutual coupling in a patch-antenna array. **e**, Full-wave simulations of the mutual coupling in the antenna array. The EBG metamaterial can suppress surface-wave propagation and mutual coupling. **f**, Comparison of the measured S parameters. The large decrease in the transmission spectra (S_{21}) indicates that the coupling current was reduced by more than 99% by the 3D printed EBG metamaterial.

self-healing ability and multiple functions using printed arc bridges and VIAs. We also created printed hemispherical helical antennas that possess smaller size, better directivity and higher sensitivity than conventional 2D patch antennas. The 3D antennas are applied to the wireless monitoring of vital signs, exhibiting high sensitivity and good agreement with a commercial ECG sensor. We also created 3D EBG metamaterials that reduce mutual coupling and enhance the performance of antenna arrays.

Comparing with previous DIW methods, CHARM3D offers several advantages, including being tension driven (with no external pressure source), fast printing speeds, free-form printing of free-standing 3D structures with an aspect ratio of up to 750:1 and no requirement for post-processing. Our current setup is limited to printing free-standing 3D architectures in a bottom-up manner, since only straight needles can fit in the vertically placed print head. However, curved needles, such as a typical curve needle bending at 45° (Supplementary Fig. 16), would theoretically enable the printing of free-standing structures in both top-down and bottom-up manners, substantially increasing the degree of freedom for creating complex 3D structures.

The printing resolution of pressure-free CHARM3D is limited to around $100\ \mu\text{m}$, as this is the point where gravity-induced inner pressure in the molten metal can still overcome the resistance of ink flowing through the nozzle tube. Smaller nozzles could theoretically offer higher resolution but would increase the resistance to be higher than gravity-induced inner pressure and thus would impede the ink

flow. Therefore, it is necessary to introduce external pressure to balance the increased resistance, if printing resolution is to be further improved. Our CHARM3D method could be used to print solid metal structures at temperatures compatible with most polymers and could assist in the development of applications such as wearable electronics, 5G technologies and the Internet of Things.

Methods

Materials

Field's metal was purchased from Roto Materials. PDMS (SYLGARD 184 silicone elastomer) was purchased from DOWSIL. The PDMS used in this work was prepared with the same ratio of 10:1. Ecoflex (00-50) was purchased from Smooth-On and utilized in the ratio of 1:1.

Printing system

The four-axis micro-positioning stage (PRO165LM, Aerotech) was driven by software (Ensemble, Aerotech). The resistance bulb-type temperature control block (TB-5E-K, Musashi Engineering) (heater) was mounted on the platform of the micro-positioning stage, whose temperature was controlled by the resistance bulb temperature controller (TCU-02, Musashi Engineering). A 5 ml stainless steel syringe (SSY-5E, Musashi Engineering) (ink barrel) with a Luer lock type was installed inside the heater. A double-thread screwed plastic nozzle with IDs of 210, 230 or $260\ \mu\text{m}$ (Musashi Engineering) was mounted on the syringe.

2D and 3D printing

Around 10 g Field's metal was loaded into the ink barrel with a mounted nozzle. Then, the ink barrel was pre-heated at the target temperature (80–100 °C) in the heater for half an hour to melt the Field's metal. To wet the new nozzle, the initiation step was conducted by pressing down the syringe head cap, which was removed after initiation, to extrude several drops of molten metal through the nozzle (Supplementary Fig. 2). After successful initiation, there was a residual metal cone remaining on the nozzle tip (Supplementary Fig. 3). The initiation was only required for the first time of a new nozzle, and the residual metal cone would be generated after every ink writing. Next, the nozzle tip was brought in close proximity to the substrate, where the distance between the nozzle tip and substrate is 100 μm ; therefore, the residual metal cone could adhere on the substrate. Then, the 2D and 3D printing processes were carried out by the micro-positioning stage according to the pre-design. The printing speeds were 20 mm s^{-1} for planar 2D printings and 1 mm s^{-1} for out-of-plane 3D printings, if not specified. To end the planar 2D printing, a high vertical speed of 30 mm s^{-1} was applied along the z axis to suddenly lift the print head, breaking the liquid wire and generating the residual metal cone on the nozzle tip. After that, the metal ink would not flow out from the nozzle as the oxide skin on the residual metal cone constrained the molten metal. To terminate the free-standing 3D printing, a high speed of 30 mm s^{-1} was applied along the direction of the last printing to generate large tension and break out the just-printed liquid filament. Normally, there might be an elongation of less than 1 mm over the designed length, which does not greatly affect the device performances or functions. The undesired elongation could be reduced by further increasing the bending speed, but unfortunately, it was impossible to eliminate the elongation for pressure-free printing. Due to its low viscosity, molten Field's metal could be easily pulled out by the large tension when terminating the printing. Theoretically, this issue can be fully addressed if an external pressure controller is employed to generate a negative pressure, which can overcome the large tension and prevent ink flow after the completion of printing.

3D printing of helical structures

The free-standing helical structures and hemispherical helical antennas were printed by coordinating the rotation of the x–y plane with the motion of the x, y and z axes. To print regular helical structures, whose diameters were constant, the x–y plane was rotating with a speed of 3.6° s^{-1} , whereas the print head was vertically listed with a speed of 10 $\mu\text{m s}^{-1}$ along the z axis. Similarly, the hemispherical helical structures were printed by coordinating the rotation of the x–y plane with the motion of y axis and the retraction of z axis. To end the printing of helical structures, a vertical high speed of 30 mm s^{-1} was applied to lift the print head along the z axis, where the printed helical structures would not deform as they could tolerate the large tension induced by the high speed owing to their spring function. All the helical structures and hemispherical helical structures were printed by the nozzle with an ID of 210 μm at 80 °C.

Fabrication of the self-healing circuit

Two serpentine wires were printed on a PDMS film with a nozzle having ID of 210 μm at 80 °C. Then, the two ends of the printed wires for connecting to the LED were heated to melt at 100 °C by a hot-air gun. Next, the LED was placed with two pads contacting the molten wires. After solidifying, the LED and printed wires were encapsulated by PDMS.

Design and fabrication of the battery-free temperature sensor system

The battery-free temperature sensor comprised an energy-harvesting antenna, a power management circuit, an LED driver integrated circuit (LM3914V, Texas Instruments) and a temperature sensor integrated circuit (LM62BIM3X, Texas Instruments). The energy-harvesting antenna

was designed with a five-turn circular shape (three turns on the top layer and two turns on the bottom layer) with a 15 mm outer radius. The line width of the antenna was 0.2 mm and the gap between the lines was 0.7 mm. An 80 pF capacitor was placed on the ends of the antenna to resonate at 13.56 MHz frequency for energy harvesting via the NFC of the mobile phone. The power management circuit was connected after the resonant capacitor to rectify the input signal to the d.c. signal. A full-bridge rectifier was formed using Schottky diodes (SMS7630-079LF, Skyworks Solutions) for rectification together with a 1 μF smoothing capacitor. The LED driver integrated circuit was designed to power one LED out of ten LEDs based on the input-temperature voltage level coming from the temperature sensor. The reference resistances were chosen to be 1.5 k Ω such that the highest-level LED would light up when the temperature is more than 90 °C and the lowest-level LED would light up when the temperature is 0 °C. The temperature step width for every LED level is 10 °C. For example, the fourth LED would light up when the temperature is between 30 and 40 °C.

To fabricate the two-layer circuit, we flipped over the whole design and manufactured it from the top layer. All the components were placed on a thin film of semi-cured PDMS according to the circuit design, and then fully encapsulated with PDMS to form a flat piece. After curing in a 70 °C oven, the thin layer of PDMS on the component pads was peeled off to expose those pads that were required for connection. To enhance adhesion, a small amount of Sn42/Bi57.6/Ag0.4 solder paste (TS391LT250, Chip Quik; melting point, 138 °C) was applied on the exposed pad with a stencil. With mild heating by a hot-air gun for 3 min, the solder paste wetted those pads and tightly bonded to them. Then, the whole piece was fixed on the micro-positioning stage and metal wires were printed by CHARM3D at a printing speed of 10 mm s^{-1} to form the coil and to connect each exposed pad according to the circuit design (Supplementary Fig. 15). Six VIAs (height, 2 mm) were printed by vertically lifting the print head from the substrate at a printing speed of 1 mm s^{-1} . Then, the whole piece was heated to 150 °C on a hotplate for 10 min to re-melt the solder paste and printed metal wires, so that they could fuse together to form a strong bonding. Those free-standing VIAs could maintain their original shape during the heat treatment owing to the solid oxide shell. Next, the printed first layer was fully encapsulated by a thin layer of PDMS, whereas the VIAs should not be submerge in PDMS. After curing the PDMS, the second layer of metal wires was printed with a printing speed of 10 mm s^{-1} to form the coil and to connect the VIAs. The print-head temperature was set at 100 °C for printing the second layer, and thus, the hot nozzle tip was able to melt the exposed areas of the VIAs to achieve robust bonding with the printed wires in the second layer. Finally, the second layer was fully encapsulated with PDMS.

Data availability

Source data are provided with this paper. Additional data related to this work are available from the corresponding authors upon request.

References

1. Zhu, Z., Ng, D. W. H., Park, H. S. & McAlpine, M. C. 3D-printed multifunctional materials enabled by artificial-intelligence-assisted fabrication technologies. *Nat. Rev. Mater.* **6**, 27–47 (2020).
2. Jung, W. et al. Three-dimensional nanoprinting via charged aerosol jets. *Nature* **592**, 54–59 (2021).
3. Zhang, Y. et al. Printing, folding and assembly methods for forming 3D mesostructures in advanced materials. *Nat. Rev. Mater.* **2**, 17019 (2017).
4. Ha, K. H. et al. Highly sensitive capacitive pressure sensors over a wide pressure range enabled by the hybrid responses of a highly porous nanocomposite. *Adv. Mater.* **33**, e2103320 (2021).
5. Tee, B. C.-K. et al. A skin-inspired organic digital mechanoreceptor. *Science* **350**, 313–316 (2015).

6. Huang, Z. et al. Three-dimensional integrated stretchable electronics. *Nat. Electron.* **1**, 473–480 (2018).
7. Liu, S., Shah, D. S. & Kramer-Bottiglio, R. Highly stretchable multilayer electronic circuits using biphasic gallium-indium. *Nat. Mater.* **20**, 851–858 (2021).
8. Valentine, A. D. et al. Hybrid 3D printing of soft electronics. *Adv. Mater.* **29**, 1703817 (2017).
9. Zhu, Z., Park, H. S. & McAlpine, M. C. 3D printed deformable sensors. *Sci. Adv.* **6**, eaba5575 (2020).
10. Truby, R. L. et al. Soft somatosensitive actuators via embedded 3D printing. *Adv. Mater.* **30**, e1706383 (2018).
11. Loke, G. et al. Structured multimaterial filaments for 3D printing of optoelectronics. *Nat. Commun.* **10**, 4010 (2019).
12. Sun, K. et al. 3D printing of interdigitated Li-ion microbattery architectures. *Adv. Mater.* **25**, 4539–4543 (2013).
13. McOwen, D. W. et al. 3D-printing electrolytes for solid-state batteries. *Adv. Mater.* **30**, e1707132 (2018).
14. Zhou, N., Liu, C., Lewis, J. A. & Ham, D. Gigahertz electromagnetic structures via direct ink writing for radio-frequency oscillator and transmitter applications. *Adv. Mater.* **29**, 1605198 (2017).
15. Adams, J. J. et al. Conformal printing of electrically small antennas on three-dimensional surfaces. *Adv. Mater.* **23**, 1335–1340 (2011).
16. Chortos, A., Hajiesmaili, E., Morales, J., Clarke, D. R. & Lewis, J. A. 3D printing of interdigitated dielectric elastomer actuators. *Adv. Funct. Mater.* **30**, 1907375 (2020).
17. Su, R., Park, S. H., Ouyang, X., Ahn, S. I. & McAlpine, M. C. 3D-printed flexible organic light-emitting diode displays. *Sci. Adv.* **8**, eabl8798 (2022).
18. Kong, Y. L. et al. 3D printed quantum dot light-emitting diodes. *Nano Lett.* **14**, 7017–7023 (2014).
19. Kim, F. et al. Direct ink writing of three-dimensional thermoelectric microarchitectures. *Nat. Electron.* **4**, 579–587 (2021).
20. Hu, J. & Yu, M. F. Meniscus-confined three-dimensional electrodeposition for direct writing of wire bonds. *Science* **329**, 313–316 (2010).
21. Zhao, J. et al. Direct coherent multi-ink printing of fabric supercapacitors. *Sci. Adv.* **7**, eabd6978 (2021).
22. Hensleigh, R. et al. Charge-programmed three-dimensional printing for multi-material electronic devices. *Nat. Electron.* **3**, 216–224 (2020).
23. Tan, Y. J. et al. A transparent, self-healing and high-kappa dielectric for low-field-emission stretchable optoelectronics. *Nat. Mater.* **19**, 182–188 (2020).
24. Yuk, H. et al. 3D printing of conducting polymers. *Nat. Commun.* **11**, 1604 (2020).
25. Molina-Lopez, F. et al. Inkjet-printed stretchable and low voltage synaptic transistor array. *Nat. Commun.* **10**, 2676 (2019).
26. Skylar-Scott, M. A., Gunasekaran, S. & Lewis, J. A. Laser-assisted direct ink writing of planar and 3D metal architectures. *Proc. Natl Acad. Sci. USA* **113**, 6137–6142 (2016).
27. Hui, Y. et al. Three-dimensional printing of soft hydrogel electronics. *Nat. Electron.* **5**, 893–903 (2022).
28. Guo, S. Z., Qiu, K., Meng, F., Park, S. H. & McAlpine, M. C. 3D printed stretchable tactile sensors. *Adv. Mater.* **29**, 1701218 (2017).
29. Ahn, B. Y. et al. Omnidirectional printing of flexible, stretchable, and spanning silver microelectrodes. *Science* **323**, 1590–1593 (2009).
30. Park, Y. G., An, H. S., Kim, J. Y. & Park, J. U. High-resolution, reconfigurable printing of liquid metals with three-dimensional structures. *Sci. Adv.* **5**, eaaw2844 (2019).
31. Ladd, C., So, J. H., Muth, J. & Dickey, M. D. 3D printing of free standing liquid metal microstructures. *Adv. Mater.* **25**, 5081–5085 (2013).
32. Gannarapu, A. & Gozen, B. A. Freeze-printing of liquid metal alloys for manufacturing of 3D, conductive, and flexible networks. *Adv. Mater. Technol.* **1**, 1600047 (2016).
33. Van Meerbeek, I. M. et al. Morphing metal and elastomer bicontinuous foams for reversible stiffness, shape memory, and self-healing soft machines. *Adv. Mater.* **28**, 2801–2806 (2016).
34. Huang, Y., Cao, Y. & Qin, H. Electric field assisted direct writing and 3D printing of low-melting alloy. *Adv. Eng. Mater.* **24**, 2200091 (2022).
35. Ren, P. & Dong, J. Direct fabrication of VIA interconnects by electrohydrodynamic printing for multi-layer 3D flexible and stretchable electronics. *Adv. Mater. Technol.* **6**, 2100280 (2021).
36. Kouraytem, N., Li, E. Q. & Thoroddsen, S. T. Formation of microbeads during vapor explosions of Field's metal in water. *Phys. Rev. E* **93**, 063108 (2016).
37. Cook, A. et al. Shear-driven direct-write printing of room-temperature gallium-based liquid metal alloys. *Adv. Eng. Mater.* **21**, 1900400 (2019).
38. Lin, J. C. Noninvasive microwave measurement of respiration. *Proc. IEEE* **63**, 1530–1530 (1975).
39. Nguyen, D. T., Zeng, Q., Tian, X. & Ho, J. S. Non-contact vital sign monitoring with a metamaterial surface. In *2022 IEEE MTT-S International Microwave Biomedical Conference (IMBioC)* 37–39 (IEEE, 2022).
40. Bland, J. M. & Altman, D. Statistical methods for assessing agreement between two methods of clinical measurement. *Lancet* **327**, 307–310 (1986).
41. Li, Z., Tian, X., Qiu, C.-W. & Ho, J. S. Metasurfaces for bioelectronics and healthcare. *Nat. Electron.* **4**, 382–391 (2021).
42. Glybovski, S. B., Tretyakov, S. A., Belov, P. A., Kivshar, Y. S. & Simovski, C. R. Metasurfaces: from microwaves to visible. *Phys. Rep.* **634**, 1–72 (2016).
43. Tian, X. et al. Wireless body sensor networks based on metamaterial textiles. *Nat. Electron.* **2**, 243–251 (2019).
44. Tian, X. et al. Implant-to-implant wireless networking with metamaterial textiles. *Nat. Commun.* **14**, 4335 (2023).
45. Stuardo, P., Pizarro, F. & Rajo-Iglesias, E. 3D-printed Sievenpiper metasurface using conductive filaments. *Materials* **13**, 2614 (2020).

Acknowledgements

B.C.K.T. acknowledges funding support from the Agency for Science Technology and Research Singapore (A*STAR) grants A20H8a0241 and A18A8b0059 and the NUS iHealthtech Institute. We thank Y. Zhao, J. Yang and S. Ong for assisting with the 3D printing and Z. J. Yang for photography. S.L. thanks S. Chang for discussions on material characterization. We also thank P. Q. Liu for assistance with the measurements in Fig. 6.

Author contributions

S.L., X.T., J.S.H. and B.C.K.T. conceived, designed and conducted the research. S.L. and Z.Q. carried out the 3D printing and FEA. Y.J.T. and J.Y.H.F. guided the 3D printing. S.L., X.T. and S.A.K. performed the design, fabrication and characterization of the 3D circuits. X.T. and Q.Z. performed the design and demonstration of the non-contact vital sign monitoring. S.L., X.T., Q.Z., S.A.K., M.D.D., J.S.H. and B.C.K.T. wrote the paper with contribution from all the authors.

Competing interests

The authors declare no competing interests.

Additional information

Supplementary information The online version contains supplementary material available at <https://doi.org/10.1038/s41928-024-01207-y>.

Correspondence and requests for materials should be addressed to John S. Ho or Benjamin C. K. Tee.

Peer review information *Nature Electronics* thanks Yong Lin Kong and Yang Yang for their contribution to the peer review of this work.

Reprints and permissions information is available at www.nature.com/reprints.

Publisher's note Springer Nature remains neutral with regard to jurisdictional claims in published maps and institutional affiliations.

Springer Nature or its licensor (e.g. a society or other partner) holds exclusive rights to this article under a publishing agreement with the author(s) or other rightsholder(s); author self-archiving of the accepted manuscript version of this article is solely governed by the terms of such publishing agreement and applicable law.

© The Author(s), under exclusive licence to Springer Nature Limited 2024